CHEMISTRY OF MATERIALS

pubs.acs.org/cm

Article

Architecting Host–Guest Synergistic Solid-State Electrolytes Enables Unobstructed Li-Ion Interphase Migration for Lithium Metal Batteries

Jingang Zheng,[†] Hao Huang,[†] Hongxu Zhou, Hongwei Zhao, Hongyang Li, Guangshen Jiang, Weichen Han, Han Zhang, Lixiang Li, Xin Geng, Baigang An,* and Chengguo Sun*

Cite This: https://doi.org/10.1021/acs.chemmater.4c02117

Read Online

ACCESS | Metrics & More | Article Recommendations | Supporting Information

ABSTRACT: Composite solid-state electrolytes inherit the intrinsic merits of each polymer and the inorganic solid-state electrolyte. However, their combined products are still unsatisfactory due to the unmatched Li-ion transport properties and the absence of structural integrity. Herein, an architectural inorganic–organic solid-state electrolyte (AIOSE) was constructed with highly coordinated Li-ion transport mode, where the primary $Li_{6.4}La_3Zr_{1.4}Ta_{0.6}O_{12}$ particles were reconstructed as a continuous fast Li-ion transport skeleton, and the assisted organic components, including poly(ethylene glycol) diacrylate, ethylene carbonate, dimethyl carbonate, and lithium difluoro(oxalato) borate, were *in situ* polymerized into an elastic fast ion filler. The principles of "host–guest synergistic regulating Li-ion transport" and "Li-ion conductivity matched in order of magnitude" can provide continuous two-phase Li-ion transfer channels, achieving a high Li-ion conductivity of 0.58 mS cm^{-1} and Li-ion transference number of 0.66 at 25 °C. The Li||AIOSE||Li symmetric cells can be cycled for 1200 h at 0.35 mA cm^{-2} without an internal short circuit and hysteresis potential rise. The Li||AIOSE||$LiNi_{0.8}Co_{0.1}Mn_{0.1}O_2$ solid-state batteries can operate properly at −20 °C with 91.6% capacity retention and maintain 1000 cycles at 20 and 60 °C with 73% capacity retention. Our fabricated strategy validates the effectiveness of the design and showcases enormous potential in solid-state lithium batteries.

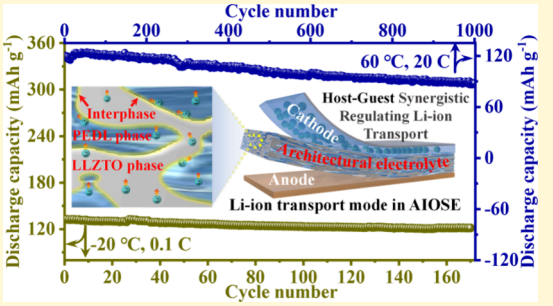

1. INTRODUCTION

Flammable organic solvents are of great concern over security issues in the technological development of Li-ion batteries. Solid-state electrolytes instead of liquid electrolytes emerged as a potential follow-up technology with higher energy and safety being much anticipated.[1−3] Among various structural configurations of solid-state electrolytes, inorganic solid-state electrolytes have excellent physicochemical stability and ultrafast Li-ion transport capability, rousing the interest of manufacturing technologies to be applied in all-solid-state lithium batteries (ASSLBs), while the poor physical contact and fragility have severely impeded the practical application.[4] In contrast, organic polymer electrolytes feature high flexibility, good capability of dissolving lithium salts, and excellent contact/adhesion with electrodes, which are supposed to make up for the demerits of inorganic electrolytes. However, the low room-temperature Li-ion conductivity is far away from the demand for ASSLBs (~10^{-4} S cm^{-1}).[5] Considering the respective merits of both inorganic and polymer electrolytes, organic–inorganic composite electrolytes (OICEs) receive great expectations to address limitations of a single component in solid-state electrolytes.[6,7] Generally, there are several structure-designed models for OICEs, including inorganic particles embedded in the organic polymer matrix,[8,9] three-dimensional (3D) inorganic networks filled with polymer,[10−12] inorganic electrolyte film surfaces coated by functionalized materials or polymer electrolytes,[13,14] and all-in-one integrated electrodes with electrolytes.[15,16] Remarkable progress on the improvement of Li-ion conductivity and optimizing the interface in OICEs has led to the record high conductivity of 10^{-4} S cm^{-1} in polymer-based electrolytes and ultralow interface impedance comparable to liquid Li-ion batteries. However, for ASSLBs with OICE, it is critical to maximize the advantages of both inorganic and polymer electrolytes with the matched Li-ion transport mode. Few design principles have been deeply considered to synergistically regulate Li-ion transport between inorganic and polymer conductors.

Most approaches only improve the Li-ion conductivity and interfacial compatibility of the solid–solid contact within the OICEs. The introduction of inorganic particles into polymer

Received: July 29, 2024
Revised: January 29, 2025
Accepted: January 29, 2025

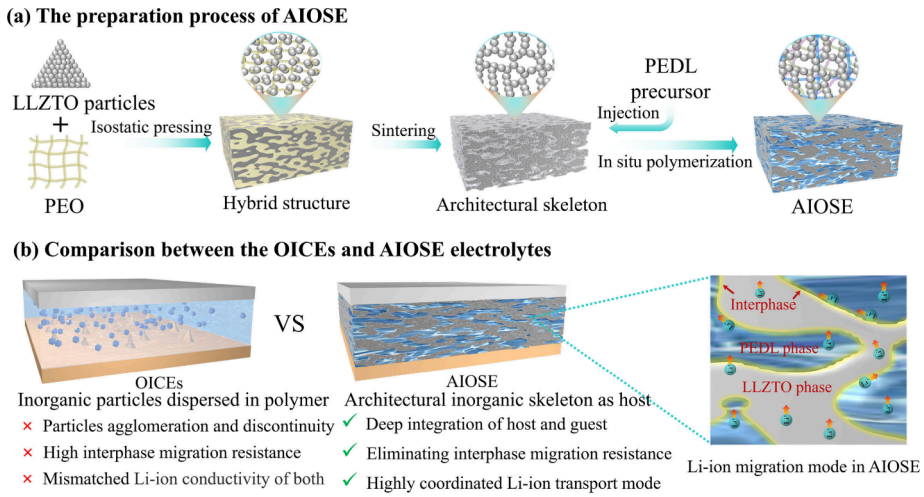

Figure 1. (a) Schematic illustration of the preparation process of AIOSE and (b) comparison of ASSLB features based on OICEs and AIOSE.

electrolytes significantly reduces the polymer crystallization and enhances the chain motility of the polymer, increasing the Li-ion conductivity up to 10^{-4} S cm^{-1} and broadening the electrochemical stabilization window over 5.0 V.[17,18] However, the nanosized inorganic particles tend to aggregate, leading to the dissatisfactory dispersion in the polymer host, hindering the formation of a percolation network throughout the polymer.[19] In contrast, 3D inorganic networks filled with polymer can greatly strengthen the interaction between inorganic and polymer electrolytes as well as form interconnected interfacial Li-ion transport channels, facilitating the rapid Li-ion conduction.[20,21] While limited by the inherent low Li-ion transport of the polymer, it is tough to achieve better ion conductivity in OICEs than that of the inborn ability of fast Li-ion transport alone in inorganic electrolytes. The strategy of surface modification technology has been adopted to elude the slow Li-ion transport in polymer electrolytes. The inorganic electrolytes surfaces coated by functionalized polymers can display high Li-ion conductivity over 10^{-4} S cm^{-1}. For example, the lithium metal anode coupled with the PPC−SN/PEO−LLZO electrolyte can form an interlayer that enhances the interfacial conductivity and electrochemical property, enabling the battery to achieve a long-term stable cycle at 0.05 mA cm^{-2} and 25 °C.[22] All of the above-mentioned strategies are aimed to use both inorganic and polymer electrolytes to make up for their respective shortcomings. Unfortunately, both advantages are not maximized from the perspective of a complete combination.

As known to all, the mechanisms of Li-ion transport in inorganic and polymer electrolytes are entirely different. The former is strongly correlated with defects of crystal structures, while the latter depends upon the segmental motion of the polymer chain. Generally, the following aspects should be simultaneously considered for designing OICEs: (1) Both inorganic and polymer electrolytes have matched Li-ion conductivity. (2) Inorganic particles should be a combination for the interaction with polymer electrolytes. (3) The content of inorganic components in OCIEs should be 2 times higher than that of organic components. (4) The good compatibility and chemical stability should be maintained between polymer and inorganic electrolytes. In fact, the fast Li-ion diffusion of OICEs involves organic−inorganic interfacial phase transfer, and from the perspective of thermodynamics, the overall Li-ion conductivity of OICEs primarily depends upon the interfacial phase with low Li-ion conductivity.[23] Limited by the low motion of the functional groups on the molecular chains, it is difficult for polymer electrolytes to possess an excellent Li-ion transport rate that matches with inorganic particles.[24] Inspired by the high Li-ion conductivity of the liquid electrolyte and solvent molecular coordination,[25] we conceived that, during the transformation of monomers to long-chain polymer molecules, the small solvent molecules can be anchored into the polymer network and assist the ion dissociation/complexation process, thus promoting the Li-ion conductivity of the polymer electrolyte.

Herein, we constructed an architectural inorganic−organic solid-state electrolyte (AIOSE) with a highly coordinated Li-ion transport mode. The primary $Li_{6.4}La_3Zr_{1.4}Ta_{0.6}O_{12}$ (LLZTO) particles were reconstructed as a continuous fast Li-ion transport skeleton (c-LLZTO) using a secondary sintering technique, providing a 3D interconnected network to increase the contact space with the polymer electrolyte. To match c-LLZTO in the fast Li-ion transport mode, the organic components (abbreviated as PEDL), including poly(ethylene glycol) diacrylate (PEGDA), ethylene carbonate (EC), dimethyl carbonate (DMC), and lithium difluoro (oxalato) borate (LiDFOB), were *in situ* polymerized in the 3D architecture of c-LLZTO to form an elastic fast ion filler. This integrated design endowed rapid transfer paths and stable permeation networks of Li-ion migration. In view of the whole structural framework, c-LLZTO acted as a host-based architecture, while polymerized PEDL was responsible for the Li-ion transport-assisted support. The whole composite solid-state electrolyte exhibited a high Li-ion conductivity of 0.58 mS cm^{-1}, which is better than that of only c-LLZTO (0.32 mS cm^{-1}) or PEDL (0.49 mS cm^{-1}). Employing AIOSE in lithium metal batteries with a $LiNi_{0.8}Co_{0.1}Mn_{0.1}O_2$ (NCM811) cathode can achieve a superhigh rate capability of 40 C at 60 °C and deliver about 66.3% of the specific capacity at −20 °C. The results provide a collaborative strategy for the design of organic−inorganic composite electrolytes in view of the structural integrity and matched Li-ion transport capacity.

https://doi.org/10.1021/acs.chemmater.4c02117
Chem. Mater. XXXX, XXX, XXX−XXX

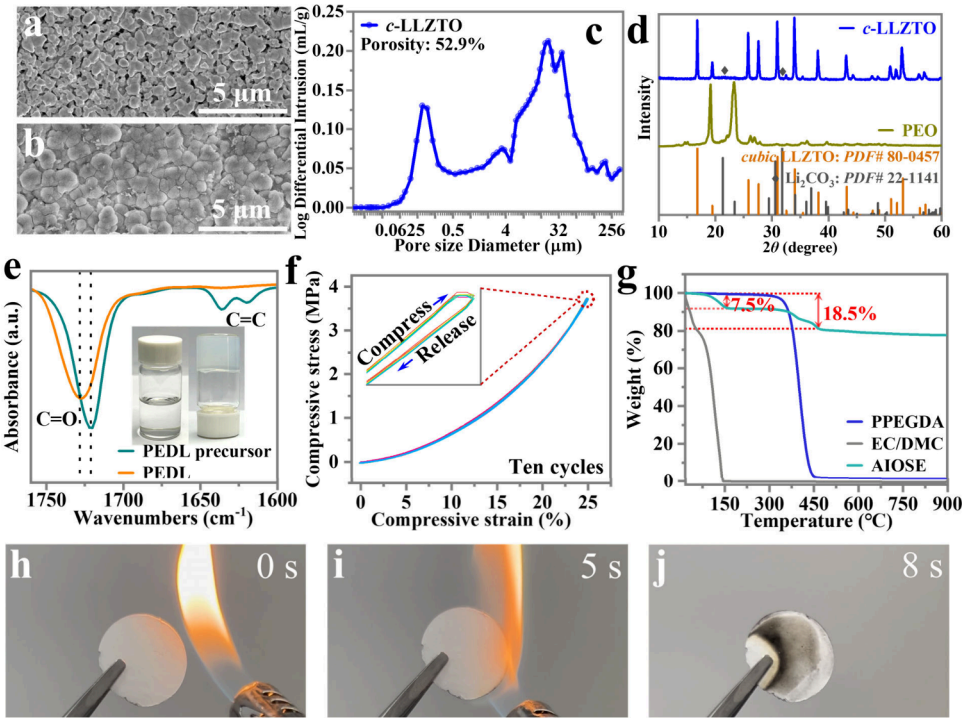

Figure 2. SEM images of (a) c-LLZTO and (b) AIOSE, (c) porosity of c-LLZTO, (d) XRD patterns of PEO and c-LLZTO, (e) FTIR spectra and digital photo of PEDL before and after heat curing, (f) compression and release tests of PEDL, (g) TGA curves of AIOSE, PPEGDA, and EC/DMC solution, and (h–j) combustion tests of AIOSE at 0, 5, and 8 s, respectively.

2. RESULTS AND DISCUSSION

2.1. Preparation of Architectural AIOSE by Secondary Poration. Figure 1a illustrates the preparation process of AIOSE and the comparison to LLZTO particles dispersed in a polymer matrix (OICEs). First, the mixture of LLZTO particles with poly(ethylene oxide) (PEO) was pressed into a sheet by cold isostatic pressure to form an integrated and dense structure. After sintering in air atmosphere at 800 °C, PEO was removed completely and the residual LLZTO particles were connected together to form a continuous c-LLZTO. It is worth mentioning that the pyrolysis of PEO will produce a rich porous structure in c-LLZTO. Second, the PEDL precursor consisting of 2.3 M LiDFOB, 1 wt % 2,2′-azobis(2-methylpropionitrile), PEGDA, and ethylene carbonate (EC)/dimethyl carbonate (DMC) (1:1, v/v, ratio) with a mass ratio of 1:5 was injected into c-LLZTO. After *in situ* polymerization of PEGDA, c-LLZTO and PEDL were closely combined into a whole electrolyte of AIOSE. In contrast to LLZTO particles dispersed in polymer electrolytes (Figure 1b), AIOSE has several advantages, including highly matched Li-ion conductivity, deep integration of the skeleton with the polymer, and integrated c-LLZTO bearing excellent interfacial stability. More importantly, integrated c-LLZTO and PEDL feature fast interfacial Li-ion exchange conduction, which effectively eliminates the interphase migration resistance.

As shown in Figure 2a, the surface of c-LLZTO reveals rich holes and an oblate particle morphology. The cross-section scanning electron microscopy (SEM) image of c-LLZTO shows that all LLZTO particles were linked together with abundant micro–nanoscale connected pores (Figure S1 of the Supporting Information). The corresponding porosity of c-LLZTO can reach as high as 52.9% (Figure 2c). After infiltration and heat curing with the PEDL precursor, the c-LLZTO surface and its internal micro–nanoscale connected pores were completely wrapped and filled with PEDL, forming a dense and integrated structure (Figure 2b and Figure S2 of the Supporting Information). The X-ray diffraction (XRD) patterns were used to analyze the structural characteristics of c-LLZTO before and after sintering. It can be found that sintered c-LLZTO is consistent with pristine LLZTO, belonging to a cubic garnet-type single-phase structure [Powder Diffraction File (PDF) 80-0457], and the PEO characteristic peaks disappear (Figure 2d). The high-resolution transmission electron microscopy (TEM) image further confirms that sintered c-LLZTO has a regular cubic phase with an exposed crystal plane (211) (Figure S3 of the Supporting Information). In addition, a layer of about 3.5 nm thickness was found on the c-LLZTO surface (Figure S3 of the Supporting Information). The enlarged view of Figure 2d shows that there are very weak characteristic peaks of Li_2CO_3 at 21.46° and 31.94°. The Raman spectra of c-LLZTO and pure LLZTO show the vibrational peak of CO_3^{2-} at 1088 cm^{-1}, and the peak intensity in c-LLZTO is higher than that in pure LLZTO (Figure S4 of the Supporting Information), which is attributed to the decomposition of PEO.[26]

The structural changes of the PEDL precursor before and after heat curing were analyzed by Fourier transform infrared spectroscopy (FTIR). As indicated in Figure 2e, the peaks at 1620 and 1636 cm^{-1} were assigned to the stretching vibration of the C=C bond in PEGDA, and after heat curing, the corresponding peaks disappeared and the C–O stretching bond shifted from 1721 to 1728 cm^{-1}, indicating that the polymerization reaction progressed well (Figure 2e and Figure S5 of the Supporting Information). To further understand the mechanical properties of polymerized PEDL, we prepared pure PEDL polymer under the same conditions. As shown in Figure 2f, PEDL can maintain the original state after 10 cycles of the compression–resilience test at a compression rate of 25%.

https://doi.org/10.1021/acs.chemmater.4c02117
Chem. Mater. XXXX, XXX, XXX–XXX

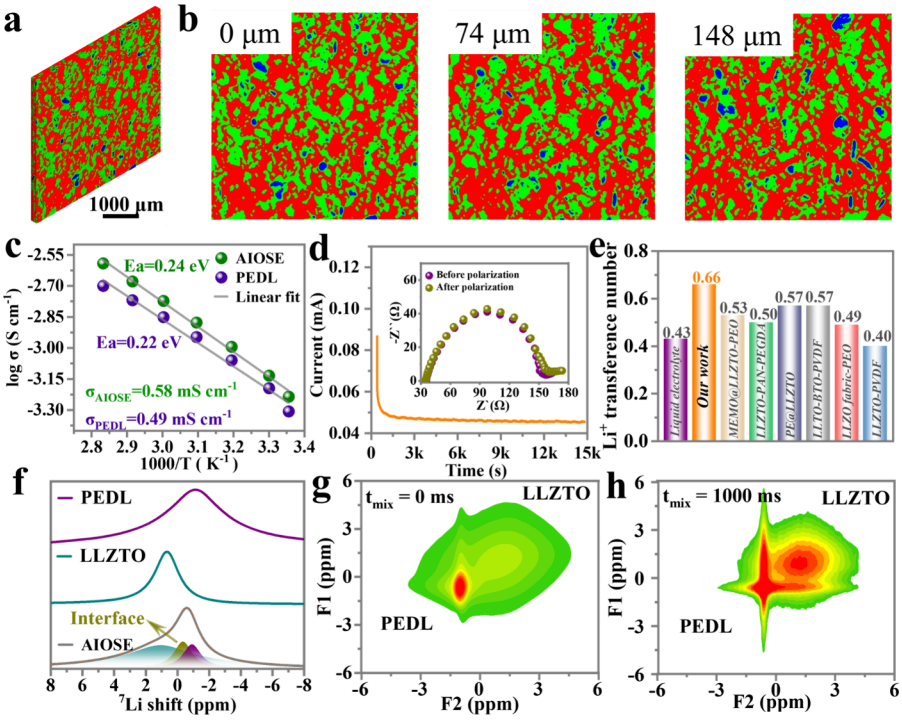

Figure 3. CT images of (a) AIOSE whole structure and (b) different depths of AIOSE, with the red, green, and blue colors corresponding to c-LLZTO, PEDL, and pores, respectively, (c) temperature-dependent Li-ion conductivity of AIOSE and PEDL electrolytes, (d) polarization curve and impedance spectra for AIOSE at 25 °C, (e) comparison of the Li-ion transference number for AIOSE with reported values based on 3D ceramic electrolytes, (f) ^{7}Li NMR curves of PEDL, LLZTO, and AIOSE, and (g and h) ^{7}Li 2D EXSY spectra of AIOSE at t_{mix} = 0 and 1000 ms.

With the further increase of the compression rate up to 41%, it still remains a complete configuration without the loss of mechanical properties (Video S1 of the Supporting Information), suggesting that PEDL has outstanding rigid−elastic balance. Figure 2g shows the thermogravimetric analysis (TGA) of AIOSE, EC/DMC solution, and pure PEGDA polymer (PPEGDA). The EC/DMC solution displays a mass loss of 100% in the range of 25−150 °C, while PPEGDA presents a single decomposition temperature over 300 °C. In contrast, the TGA curve for AIOSE is divided into three distinct plateaus. The first step begins to lose the EC/DMC mixture between 100 and 160 °C (Figure S6 of the Supporting Information), which is much higher than that observed for pure EC/DMC solution, indicating the strong intermolecular force between EC/DMC molecules and PPEGDA chains/lithium salts. In other words, there are no free EC/DMC solvent molecules existing in AIOSE. In the decomposition step between 320 and 500 °C, the weight loss reached 11%, which is related to the decomposition of PPEGDA and LiDFOB. Taken as a whole, we concluded that the content of LLZTO in AIOSE is as high as 81.5%. As a result, in the case of continuous ignition by an external fire source, AIOSE exhibits non-flammable behavior (panels h−j of Figure 2). In contrast, both PEDL and EC/DMC absorbed on glass fibers can be easily ignited (Figure S7 of the Supporting Information).

2.2. Host−Guest Synergistic Regulating Li-Ion Transport Mechanism. X-ray computed tomography (CT) was employed to visualize the component distribution in AIOSE. As shown in panels a and b of Figure 3, PEDL completely penetrated into c-LLZTO to form a uniform and dense structure. The result is further evidenced by the CT images of the c-LLZTO skeleton and PEDL in the AIOSE electrolyte (Figure S8 of the Supporting Information). With the depth of the cross-section from 0 μm (surface) to 74 μm ($^{1}/_{4}$) to 148 μm ($^{1}/_{2}$), a few pores gradually appeared, and the overall porosity is only 4.6% (Figure S9 of the Supporting Information). Electrochemical tests were used to analyze the synergistic effects of Li-ion transport in AIOSE. Under the same test conditions, the Li-ion conductivity of c-LLZTO is up to 0.32 mS cm^{-1} at 25 °C, slightly higher than that of 0.26 mS cm^{-1} for pure LLZTO (Figure S10 of the Supporting Information). Considering the additional support function of c-LLZTO in AIOSE, a Celgard 2500 separator was employed instead of c-LLZTO to combine with PEDL, and the room-temperature Li-ion conductivity is 0.49 mS cm^{-1}. As expected, after the combination of c-LLZTO with PEDL, the Li-ion conductivity of AIOSE is as high as 0.58 mS cm^{-1} (Figure 3c and Figure S11 of the Supporting Information), indicating that both PEDL and c-LLZTO contribute to ion transport in the composite electrolyte.

The calculated activation energies (E_a) of PEDL and AIOSE are 0.22 and 0.24 eV, respectively, which are much lower than those reported for LLZTO-based electrolytes (0.28−0.38 eV) (Figure S12 of the Supporting Information). The lower E_a can reduce the temperature dependence of Li-ion conductivity for AIOSE.[27] As shown in Figure 3d, the calculated Li-ion transference number of AIOSE is as high as 0.66, exceeding the liquid electrolytes of 0.43 and that of most reported composite electrolytes (Figure 3e).[1,28−32] The above results demonstrate that PEDL and c-LLZTO play a synergistic effect in promoting Li-ion migration in AIOSE. To further investigate the ion transport process in AIOSE, the ^{7}Li solid-state nuclear magnetic resonance (SSNMR) technique was employed to analyze the local chemical environment of the Li-ion. As shown in Figure 3f, the peak positions of the Li-ion for PEDL and

https://doi.org/10.1021/acs.chemmater.4c02117
Chem. Mater. XXXX, XXX, XXX−XXX

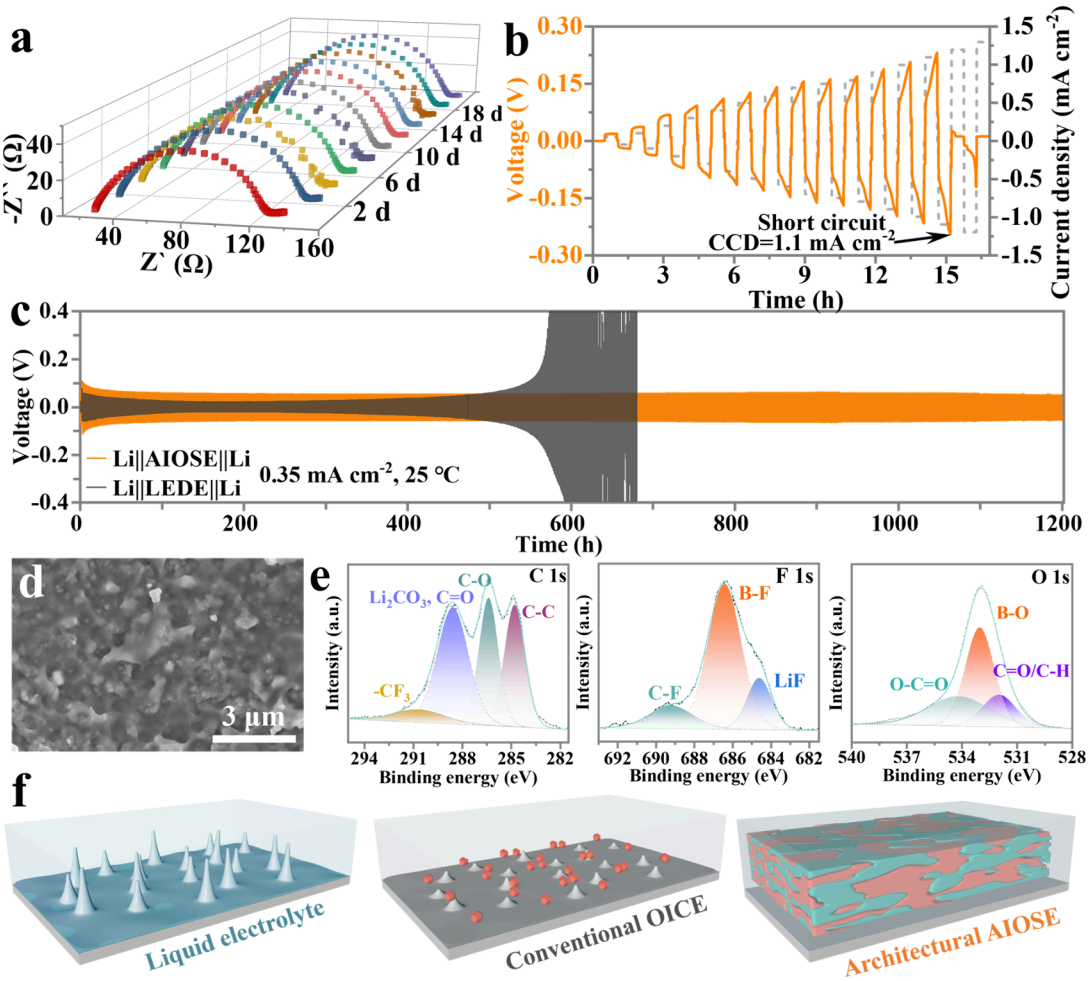

Figure 4. (a) Time-evolution EIS plots of the Li||AIOSE||Li cell, (b) critical current density test of AIOSE, (c) galvanostatic curves of Li||AIOSE||Li and Li||LEDE||Li cells, (d) SEM image of lithium metal disassembled from NCM811||AIOSE||Li cells after 100 cycles at 2 C, (e) XPS spectra (C 1s, F 1s, and O 1s) of lithium metal disassembled from NCM811||AIOSE||Li cells after 100 cycles at 2 C, and (f) schematic diagram of dendrite growth suppression in different electrolyte systems.

LLZTO phase are located at −1.07 and 0.96 ppm, respectively, while the SSNMR spectrum of AIOSE shows a new peak at −0.37 ppm, corresponding to the chemical environment of the Li-ion at the interface, suggesting that the diffusion paths of the Li-ion change properly and a large number of Li-ions can freely migrate across the interface. The two-dimensional (2D) NMR spectra of ^{7}Li were used to further observe the exchange of multiple lithium sites between different chemical environments. At the mixing time t_{mix} = 0 ms, the signals were mainly concentrated in the PEDL phase (Figure 3g). Once the mixing time was extended to 1000 ms, the signal intensity for the LLZTO phase and interfacial phase gradually increased (Figure 3h), which indicates that the Li ion underwent a rapid exchange reaction at the interfacial phase.

2.3. Compatibility of the Electrolyte−Electrode Interfaces. The stability of the AIOSE−Li anode interface was evaluated using a static interfacial impedance test (Figure 4a). Over a period of 20 days, the impedance value increased from 134.5 to 155.1 Ω, with an average increase of only 1.03 Ω per day. The result is much lower than the reported increase of ∼100 Ω over 120 h,[33] exhibiting that AIOSE has excellent chemical stability and interfacial affinity with lithium metal. Further evidence can be found from a high critical current density of 1.1 mA cm^{-2} (Figure 4b), which is comparable to that of reported LLZTO-based electrolytes. At different current densities, Li||AIOSE||Li cells exhibit low overpotential plateaus of 34.7, 53.8, 67.1, and 107.8 mV at 0.15, 0.35, 0.45, and 0.65 mA cm^{-2}, respectively (Figure S13 of the Supporting Information). At 0.35 mA cm^{-2}, the cell can maintain stable cycling over 1200 h without an internal short circuit and a rise in hysteresis potential (Figure 4c). In contrast, the lithium symmetric cell assembled with a conventional liquid electrolyte (1 M $LiPF_6$−EC/DEC/EMC, abbreviated as LEDE) is short-circuited for less than 500 cycles due to the instability of the interface and the growth of lithium dendrites. As shown in Figure 4d, the SEM image of lithium deposited from the NCM811||AIOSE||Li cell shows a dense, uniform, and dendrite-free morphology, while a loose and porous lithium deposition is observed from the NCM811||LEDE||Li cell (Figure S14a of the Supporting Information). Figure 4e shows the X-ray photoelectron spectroscopy (XPS) spectra of the lithium metal anode obtained from the cycled NCM811||AIOSE||Li cell. In the C 1s spectrum, three peaks at 288.58, 286.36, and 284.79 eV are indicative of Li_2CO_3,[34] and three peaks at 689.29, 684.63, and 686.43 eV in the F 1s spectrum, corresponding to C−F, Li−F, and B−F bonds, are associated with $DFOB^-$ anion decomposition. In the O 1s spectrum, three peaks at 534.24, 533.05, and 531.97 eV can be assigned

https://doi.org/10.1021/acs.chemmater.4c02117
Chem. Mater. XXXX, XXX, XXX−XXX

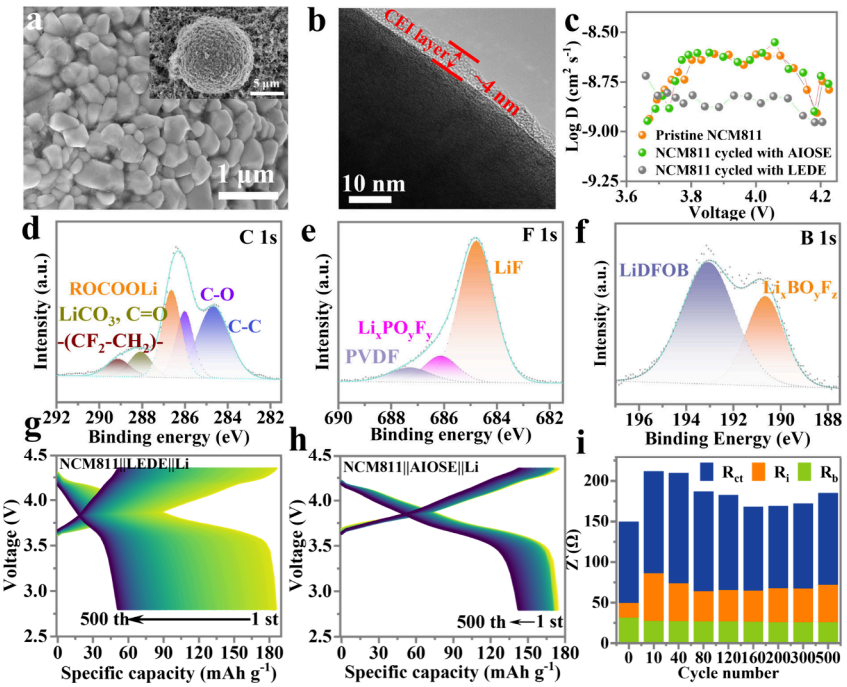

Figure 5. (a) SEM and (b) TEM images of NCM811 particles disassembled from the cycled NCM811||AIOSE||Li cell, (c) $D_{Li\text{-}ion}$ of pristine NCM811 and NCM811 cycled with AIOSE and LEDE at 2 C for 100 cycles, (d–f) XPS analysis of C 1s, F 1s, and B 1s spectra for NCM811 cycled with AIOSE, (g and h) charge–discharge curves of NCM811||LEDE||Li and NCM811||AIOSE||Li cells at 1 C and 25 °C, and (i) impedance values of R_{ct}, R_i, and R_b for NCM811||AIOSE||Li cells after different cycles.

to the anion in $DFOB^-$ decomposition and the organic component of the solid electrolyte interface (SEI) layer. The aforementioned results demonstrate that LiDFOB is mainly involved in constructing the stably dense SEI. In contrast, the surface of the lithium metal anode disassembled from the cycled NCM811||LEDE||Li cell mainly consists of organic species due to the decomposition of $LiPF_6$ (Figure S14b of the Supporting Information). As expected, after 100 cycles of lithium deposition/stripping at 0.5 mA cm^{-2}, the average coulombic efficiency (CE_{avg}) of the Li||AIOSE||Cu cell is as high as 96.31%, while CE_{avg} of the cell with the LEDE electrolyte fluctuates and fades out after 30 cycles (Figure S15 of the Supporting Information). The above evidence suggests that LiDFOB can boost the LiF content by self-decomposition, thereby creating a more robust SEI layer on the Li metal anode surface.[35,36] The combined action of architectural AIOSE and robust SEI layer is critical in guiding the horizontal deposition of lithium, thus inhibiting the lithium dendrite growth under a high current density and long-term cycling (Figure 4f).

As for the cathode electrolyte interphase (CEI) layer, the morphology of the NCM811 electrode before and after cycling was observed. As shown in Figure 5a, the NCM811 particles disassembled from the cycled NCM811||AIOSE||Li cells were clearly visible in the contours, which is consistent with the morphology of the original NCM811 particles (Figure S16a of the Supporting Information). In contrast, the morphology of NCM811 particles from the NCM811||LEDE||Li cell is partly broken, and the surface contours become blurred (Figure S16b of the Supporting Information). The TEM images further reveal that the CEI layer of NCM811 cycled with AIOSE is uniform and approximates 4 nm (Figure 5b), which is far lower than that of 17 nm for the cycled cell with LEDE (Figure S17 of the Supporting Information). The XPS measurement was conducted to further determine the composition of the CEI layers. As seen in panels d–f of Figure 5, the C 1s, F 1s, and B 1s spectra of NCM811 cycled with AIOSE can be divided into several important peaks for CEI, including ROCOOLi (286.62 eV, C 1s), LiF (684.77 eV, F 1s), and $Li_xBO_yF_z$ (190.66 eV, B 1s). However, apart from the above-mentioned components, new products of Li_xPF_y (687.84 eV, F 1s) and PF_5 (686.06 eV, F 1s) decomposed by $LiPF_6$ were also found in the F 1s spectrum of NCM811 cycled with LEDE (Figure S18 of the Supporting Information). The products will corrode the CEI components, leading to continuous structural decay of the NCM811 cathode.[37] The Li-ion diffusion coefficients ($D_{Li\text{-}ion}$) of NCM811 cycled with AIOSE and LEDE were further calculated by the galvanostatic intermittent titration technique (GITT) curves. As shown in Figure 5c, after 100 cycles at 2 C, $D_{Li\text{-}ion}$ of NCM811 cycled with AIOSE shows no obvious change compared to pristine NCM811, and the discharge capacity of 193.7 mAh g^{-1} is still close to the theoretical value (1 C = 200 mA g^{-1}). On the contrary, $D_{Li\text{-}ion}$ of NCM811 cycled with LEDE is significantly decreased, and the capacity is consequently reduced to 150 mAh g^{-1} (Figure S19 of the Supporting Information). Meanwhile, the wide electrochemical stability window of AIOSE is up to 5.6 V (Figure S20 of the Supporting Information); thus, the NCM811||AIOSE||Li cell exhibits excellent cycling stability with a very small capacity decay of 0.036% per cycle in the first 500 cycles (Figure 5h), much lower than that of 0.143% for the NCM811||LEDE||Li cell (Figure 5g).

Figure S21 of the Supporting Information displays the electrochemical impedance spectroscopy (EIS) curves and the corresponding equivalent circuit model of NCM811||AIOSE|| Li cells under different cycles at 2 C and 25 °C. The fitted impedance data, including the bulk electrolyte (R_b), interface resistance (R_i), and charge transfer resistance (R_{ct}) for 0th, 10th, 40th, 80th, 120th, 160th, 200th, 300th, and 500th cycles,

https://doi.org/10.1021/acs.chemmater.4c02117
Chem. Mater. XXXX, XXX, XXX−XXX

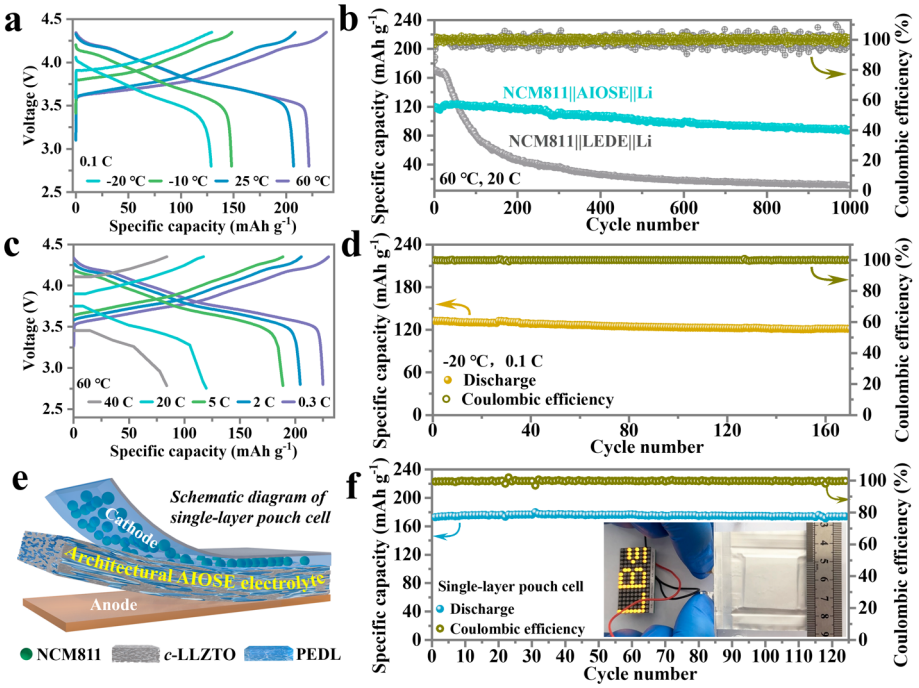

Figure 6. (a) Charge and discharge curves of NCM811||AIOSE||Li cells in the range from −20 to 60 °C at 0.1 C, (b) cycling stability of NCM811||AIOSE||Li and NCM811||LEDE||Li cells at 20 C and 60 °C, (c) charge and discharge curves of NCM811||AIOSE||Li cells from 0.3 to 40 C at 60 °C, (d) cycling stability of the NCM811||AIOSE||Li cell at 0.1 C and −20 °C, (e) schematic diagram of the single-layer NCM811||AIOSE||Li pouch cell, and (f) cycling stability of the pouch cell at 0.2 C and 25 °C, with the pouch cell lighting up an 8 × 16 LED dot matrix.

are shown in Figure 5i. Before charging, R_b was 31.54 Ω; after 500 cycles, it stabilized between 25.87 and 27.34 Ω. R_{ct} is increased from 100.3 to 113.3 Ω during the cycling process. From 0 to 10 cycles, R_i increased from 18.16 to 58.88 Ω and was then maintained steady at 40−46 Ω from the 10th to 500th cycles. The increase in R_i during the initial 10 cycles can be attributed to the sacrifice of the electrolyte components to form a CEI layer. R_i decreased and remained stable in the subsequent cycles, indicating that the CEI layer has a good mechanical strain property to maintain the mechanical integrity of the electrode structure and high interfacial stability during cycling.

To further reveal the synergistic interaction between architectural c-LLZTO and PEDL for the promotion of battery performances, the solid-state electrolyte with a similar structural configuration were prepared using the Al_2O_3 skeleton and Celgard 2500 separator instead of c-LLZTO and c-LLZTO filled with liquid LEDE. It can be found that the cell with LEDE shows a high initial discharge specific capacity of 175.9 mAh g^{-1} at 2 C (Figure S22 of the Supporting Information). Unfortunately, the discharge specific capacity shows a cliff-like capacity drop after 50 cycles, and only 23.1 mAh g^{-1} capacity is maintained after 1000 cycles. Other cells using the Celgard 2500−PEDL and c-LLZTO−LEDE electrolytes show almost the same decay trend. It is worth mentioning that the cell with the Al_2O_3 skeleton−PEDL electrolyte hardly charges and discharges even at 0.1 C. The results prove that, in AIOSE, c-LLZTO works as a host for ion transport, PEDL is invented as an auxiliary guest, and both c-LLZTO and PEDL work synergistically to accelerate Li-ion migration. This is further confirmed by the cross-sectional SEM image of AIOSE cycled with NCM811 (Figure S23 of the Supporting Information), where PEDL keeps the original features in the c-LLZTO skeleton without being consumed during cycling.

2.4. Electrochemical Performances of Lithium Metal Batteries in Wide Temperatures. Figure 6a presents the voltage curves of the NCM811||AIOSE||Li cell in the range from −20 to 60 °C at 0.1 C. The high discharge specific capacity is 207.1 mAh g^{-1} at 25 °C and 224.9 mAh g^{-1} at 60 °C. Even at −10 and −20 °C, it can still provide an excellent discharge specific capacity of 148.1 and 128.7 mAh g^{-1}, respectively. As for the rate performances, the NCM811||AIOSE||Li cell exhibits a high discharge specific capacity of 205.7, 190.5, 163.7, 141.1, and 105.5 mAh g^{-1} at 0.1, 1, 3, 5, and 10 C, respectively. When the current density is switched back to 0.1 C, the capacity is restored to 203.2 mAh g^{-1} (Figure S24 of the Supporting Information). With a further increase of the temperature to 60 °C, the cell shows a high-rate capability with a discharge specific capacity of 221.7, 204.4, 188.8, 119.7, and 84.0 mAh g^{-1} at 0.3, 2, 5, 20, and 40 C, respectively (Figure 6c). After long-term cycling at 20 C, the cell maintains a stable cycle of up to 1000 cycles with a high initial discharge capacity of 120.8 mAh g^{-1} and satisfactory capacity retention rate of 73% (Figure 6b). With the further increase of the rate to 40 C, it still exhibits a high CE_{avg} of 99.65% (Figure S25 of the Supporting Information). More importantly, the NCM811||AIOSE||Li cell also provides a high initial discharge specific capacity of 132.6 mAh g^{-1} at 0.1 C and −20 °C and retains an outstanding capacity retention of 91.6% after 170 cycles (Figure 6d). The outstanding wide-temperature performances and high-voltage stability are superior to those reported in the literature (Figure S26 of the Supporting Information). To further investigate the suitability between AIOSE and commercial cathode materials, the cells using AIOSE and lithium metal were assembled with $LiFePO_4$ and $LiNi_{0.6}Mn_{0.2}Co_{0.2}O_2$ (NCM622) cathodes. As a result, both types of cells maintain excellent cycling stability at 2 C and 25 °C, where the capacity retention after 500 cycles is

https://doi.org/10.1021/acs.chemmater.4c02117
Chem. Mater. XXXX, XXX, XXX−XXX

96.1 and 85.8%, respectively (Figure S27 of the Supporting Information). Figure 6e shows the applications of the AIOSE electrolyte in a single-layer Li||NCM811 pouch cell. The discharge specific capacities of the pouch cell at 0.1, 0.2, 0.3, and 0.5 C were 182.9, 176.6, 171.4, and 161.0 mAh g^{-1}, respectively (Figure S28 of the Supporting Information). Moreover, it can maintain a discharge specific capacity of 173.9 mAh g^{-1} after 124 cycles without obvious capacity decay at 0.2 C and 25 °C (Figure 6f). The capacity utilization and cycle life of the AIOSE-based pouch cell are superior to those recently reported for 3D LLZTO-based composite solid electrolytes (Table S1 of the Supporting Information). As expected, a fully charged NCM811||AIOSE||Li pouch cell successfully lights the 8 × 16 light-emitting diode (LED) dot matrix. All of above-mentioned results illustrate that the design of host−guest synergistic regulating Li-ion transport in architectural composite solid-state electrolytes is an effective combination strategy for high-performance solid-state batteries.

3. CONCLUSION

In summary, AIOSE with matched ion-transport efficiency and cooperative regulation function was obtained through the sintering reconfigured c-LLZTO host and PEDL-assisted support. With the inherent matched Li-ion conductivity of c-LLZTO (0.32 mS cm^{-1}) and PEDL (0.49 mS cm^{-1}) as well as the deep integration between the rigid host and flexible guest, AIOSE delivers a high room-temperature Li-ion conductivity (0.58 mS cm^{-1}) and robust electrode−electrolyte interfaces. In the cycle test of lithium symmetric batteries, the AIOSE-based battery achieves excellent cycling stability over 1200 h at 0.35 mA cm^{-2}. As a result, the NCM811||AIOSE||Li cells exhibit prominent rate performance, cycling stability, and smooth operation in wide temperatures. Furthermore, the AIOSE-based pouch cell can be cycled stably at 0.2 C and 25 °C without obvious capacity decay. This customized architectural strategy for the composite solid-state electrolyte with highly matched ion transport rates can be a promising technology for ASSLBs with wide-temperature operability as well as address the issues of high-voltage cathode suitability and electrode−electrolyte interfaces.

4. EXPERIMENTAL SECTION

4.1. Preparation of AIOSE. *4.1.1. Preparation of c-LLZTO.* $Li_{6.4}La_3Zr_{1.4}Ta_{0.6}O_{12}$ (LLZTO, with an average particle size of 500 nm) was mixed with poly(ethylene oxide) (PEO, M_w = 600 000, Sigma-Aldrich) in the mass ratio of 20:3 by high-speed ball milling. After that, the above mixture was pressed into a 16 mm diameter pellet using a hydraulic press to obtain a hybrid structure and then sintered at 800 °C for 2 h with a heating rate of 10 °C min^{-1} in an air atmosphere. The sintered sample is named c-LLZTO, and the thickness is about 300 μm. After sintering, c-LLZTO was quickly transferred to the glovebox (H_2O < 0.1 ppm and O_2 < 0.1 ppm) under an Ar atmosphere for backup.

4.1.2. Preparation of the PEDL Precursor. EC/DMC (1:1, v/v) and polyethylene glycol diacrylate (PEGDA, M_n ~ 400) were used in a 5:1 mass ratio and 2.3 M LiDFOB to form the PEDL precursor solution. At 10 min before using it, 1% 2,2′-azobis(2-methylpropionitrile) (relative to the mass of PEGDA) was added as a heat-curing initiator.

4.1.3. Preparation of AIOSE. c-LLZTO was immersed in the PEDL precursor for 10 min at a pressure of 0.6 MPa, aiming to fully fill the pores of c-LLZTO with the PEDL precursor, and then the cell was assembled, with *in situ* heat curing of PEGDA.

4.2. Assembly of ASSLBs. Commercial cathode powders (including $LiFePO_4$, NCM622, and NCM811), Super-P, and polyvinylidene fluoride (PVDF) were mixed in *N*-methyl pyrrolidone solution in the mass ratio of 8:1:1, respectively. After mixing, the slurry was scraped onto the aluminum foil using the tape-casting method and cut into 12 mm diameter tablets for coin cells and 3 × 3 cm^2 sizes for single-layer pouch cells, respectively. The cells were assembled in a glovebox under an Ar atmosphere, where stainless steel, lithium pellets, or a 10 μm thick lithium sheet was used as the anode material. The cathode mass loading was about 1.8−2.0 mg cm^{-2}.

4.3. Physical Characterization. Scanning electron microscopy (Apreo S, FEI) was used to obtain the surface and cross-section morphologies of c-LLZTO and AIOSE. X-ray photoelectron spectroscopy was measured by AXIS-SUPRA, KRATOS. XRD and FTIR were measured by D8 with Cu Kα radiation and ALPHA II, Bruker Corporation. The X-ray computed tomography was performed by skysCan2211 with a scanning voltage of 60 kV. The ^{7}Li magic angle spinning (MAS) experiments were carried out on Bruker Avance Neo 400WB operating at 155.6 MHz for ^{7}Li. A 3.2 mm double-resonance MAS probe was employed. The recycle delay was 10.0 s. For the 2D ^{7}Li exchange NMR experiment, the exchange time was set to 0 and 1000 ms. The ^{7}Li chemical shift was calibrated using 1 M LiCl solution = 0 ppm for ^{7}Li.

4.4. Electrochemical Characterization. The charge−discharge tests are conducted from −20 to 60 °C with the voltage ranging from 2.5 to 4.2 V for Li||$LiFePO_4$, from 2.8 to 4.3 V for Li||NCM622, and from 2.8 to 4.35 V for Li||NCM811 cells, respectively. The Li||AIOSE||Li cells were used to measure the Li plating/stripping with a constant current charge for 30 min, then discharge for 30 min, and so on. EIS was also taken for Li||AIOSE||Li cells before and after direct-current polarization. The Li-ion conductivity (σ) of PEDL, AIOSE, pure LLZTO, and c-LLZTO were measured by an alternating current (AC) impedance technique at various temperatures ranging from 25 to 80 °C. All EIS measurements were carried out on a VSP300 (Biologic) workstation over the frequency from 3 MHz to 0.1 Hz with an amplitude of 10 mV at room temperature.

The Li-ion conductivity was calculated from the following equation:

$$\sigma = \frac{d}{SR_b}$$

where d (cm) is the thickness of AIOSE, S (cm^2) is the area of the stainless-steel electrode, and R_b (Ω) is the bulk resistance of the electrolyte membrane measured by EIS.

The Li-ion transference number (t^+) of the solid electrolyte was measured using the chronoamperometry test on the Li||AIOSE||Li cell with an applied voltage of 10 mV, and t^+ was calculated by the following equation:

$$t^+ = \frac{I_s(\Delta V - I_0R_0)}{I_0(\Delta V - I_sR_s)}$$

where ΔV (V) is the potential applied across the cell, and the initial (I_0) and steady-state (I_s) currents were obtained from the chronoamperometric curves. R_0 and R_s measured by EIS reflect the initial and steady-state resistances of AIOSE.

■ ASSOCIATED CONTENT

Supporting Information

The Supporting Information is available free of charge at https://pubs.acs.org/doi/10.1021/acs.chemmater.4c02117.

PEDL still remains a complete configuration without the loss of mechanical properties with the further increase of the compression rate up to 41%, suggesting that it has outstanding rigid−elastic balance (Video S1) (MP4)

Summary of the electrochemical performances, SEM images, XPS spectra, and TEM images (PDF)

https://doi.org/10.1021/acs.chemmater.4c02117
Chem. Mater. XXXX, XXX, XXX−XXX

AUTHOR INFORMATION

Corresponding Authors

Baigang An − *School of Chemical Engineering, University of Science and Technology Liaoning, Anshan, Liaoning 114051, People's Republic of China;* orcid.org/0000-0001-6111-8166; Email: bgan@ustl.edu.cn

Chengguo Sun − *School of Chemical Engineering, University of Science and Technology Liaoning, Anshan, Liaoning 114051, People's Republic of China; School of Chemical Engineering, Nanjing University of Science and Technology, Nanjing, Jiangsu 210094, People's Republic of China;* orcid.org/0000-0003-3580-2153; Email: sunyangguo2004@163.com

Authors

Jingang Zheng − *School of Chemical Engineering, University of Science and Technology Liaoning, Anshan, Liaoning 114051, People's Republic of China*

Hao Huang − *School of Chemical Engineering, University of Science and Technology Liaoning, Anshan, Liaoning 114051, People's Republic of China*

Hongxu Zhou − *School of Chemical Engineering, University of Science and Technology Liaoning, Anshan, Liaoning 114051, People's Republic of China*

Hongwei Zhao − *School of Chemical Engineering, University of Science and Technology Liaoning, Anshan, Liaoning 114051, People's Republic of China*

Hongyang Li − *School of Chemical Engineering, University of Science and Technology Liaoning, Anshan, Liaoning 114051, People's Republic of China*

Guangshen Jiang − *School of Chemical Engineering, University of Science and Technology Liaoning, Anshan, Liaoning 114051, People's Republic of China;* orcid.org/0000-0001-9213-1515

Weichen Han − *School of Chemical Engineering, University of Science and Technology Liaoning, Anshan, Liaoning 114051, People's Republic of China*

Han Zhang − *School of Chemical Engineering, University of Science and Technology Liaoning, Anshan, Liaoning 114051, People's Republic of China;* orcid.org/0000-0001-6905-0952

Lixiang Li − *School of Chemical Engineering, University of Science and Technology Liaoning, Anshan, Liaoning 114051, People's Republic of China*

Xin Geng − *School of Chemical Engineering, University of Science and Technology Liaoning, Anshan, Liaoning 114051, People's Republic of China*

Complete contact information is available at: https://pubs.acs.org/10.1021/acs.chemmater.4c02117

Author Contributions

†Jingang Zheng and Hao Huang contributed equally to this work. Jingang Zheng and Hao Huang, methodology, writing—original draft, and data curation; Hongxu Zhou, data curation and formal analysis; Hongwei Zhao, investigation and validation; Xin Geng and Hongyang Li, investigation; Lixiang Li, conceptualization and visualization; Guangshen Jiang and Baigang An, supervision; Weichen Han and Han Zhang, validation and visualization; Jingang Zheng and Chengguo Sun, writing—review and editing; and Baigang An and Chengguo Sun, supervision, funding acquisition, and validation.

Notes

The authors declare no competing financial interest.

ACKNOWLEDGMENTS

The authors gratefully acknowledge financial support by the National Natural Science Foundation of China (11972178, 22109061, and 52371224) and the Natural Science Foundation of Liaoning Province (2023-BS-184).

REFERENCES

(1) Shi, P.; Ma, J.; Liu, M.; Guo, S.; Huang, Y.; Wang, S.; Zhang, L.; Chen, L.; Yang, K.; Liu, X.; Li, Y.; An, X.; Zhang, D.; Cheng, X.; Li, Q.; Lv, W.; Zhong, G.; He, Y.-B.; Kang, F. A Dielectric Electrolyte Composite with High Lithium-Ion Conductivity for High-Voltage Solid-State Lithium Metal Batteries. *Nat. Nanotechnol.* **2023**, *18*, 602−610.

(2) Janek, J.; Zeier, W. G. Challenges in Speeding up Solid-State Battery Development. *Nat. Energy.* **2023**, *8*, 230−240.

(3) Liang, Y.; Kerr, R.; Wang, X.; Ueda, H.; Armand, M.; Forsyth, M.; Howlett, P. C. New Plastic Crystal Composite Electrodes Employing Delocalized Transition Metal Salts for Low-Cost, High-Safety All-Solid-State Salt Batteries. *Chem. Mater.* **2024**, *36*, 7222−7231.

(4) Chen, X.; Guan, Z.; Chu, F.; Xue, Z.; Wu, F.; Yu, Y. Air-Stable Inorganic Solid-State Electrolytes for High Energy Density Lithium Batteries: Challenges, Strategies, and Prospects. *InfoMat* **2022**, *4* (1), No. e12248.

(5) Yang, M.; Epps, T. H., III Solid-State, Single-Ion Conducting, Polymer Blend Electrolytes with Enhanced Li^+ Conduction, Electrochemical Stability, and Limiting Current Density. *Chem. Mater.* **2024**, *36*, 1855−1869.

(6) Liang, H.; Wang, L.; Wang, A.; Song, Y.; Wu, Y.; Yang, Y.; He, X. Tailoring Practically Accessible Polymer/Inorganic Composite Electrolytes for All-Solid-State Lithium Metal Batteries: A Review. *Nano-Micro Lett.* **2023**, *15*, 42.

(7) Xue, S.; Chen, S.; Fu, Y.; Zhu, H.; Ji, Y.; Song, Y.; Pan, F.; Yang, L. Revealing the Role of Active Fillers in Li-Ion Conduction of Composite Solid Electrolytes. *Small.* **2023**, *19*, No. 2305326.

(8) Liu, S.; Liu, W.; Ba, D.; Zhao, Y.; Ye, Y.; Li, Y.; Liu, J. Filler-Integrated Composite Polymer Electrolyte for Solid-State Lithium Batteries. *Adv. Mater.* **2023**, *35* (2), No. 2110423.

(9) Liu, M.; Zhang, S.; van Eck, E. R. H.; Wang, C.; Ganapathy, S.; Wagemaker, M. Improving Li-Ion Interfacial Transport in Hybrid Solid Electrolytes. *Nat. Nanotechnol.* **2022**, *17*, 959−967.

(10) Alexander, G. V.; Shi, C.; O'Neill, J. E.; Wachsman, D. Extreme Lithium-Metal Cycling Enabled by a Mixed Ion and Electron-Conducting Garnet Three-Dimensional Architecture. *Nat. Mater.* **2023**, *22*, 1136−1143.

(11) Bao, C.; Zheng, C.; Wu, M.; Zhang, Y.; Jin, J.; Chen, H.; Wen, Z. 12 μm-Thick Sintered Garnet Ceramic Skeleton Enabling High-Energy-Density Solid-State Lithium Metal Batteries. *Adv. Energy Mater.* **2023**, *13*, No. 2204028.

(12) Guo, D.; Shinde, D. B.; Shin, W.; Abou-Hamad, E.; Emwas, A.-H.; Lai, Z.; Manthiram, A. Foldable Solid-State Batteries Enabled by Electrolyte Mediation in Covalent Organic Frameworks. *Adv. Mater.* **2022**, *34*, No. 2201410.

(13) Zhao, B.; Ma, W.; Li, B.; Hu, X.; Lu, S.; Liu, X.; Jiang, Y.; Zhang, J. A Fast and Low-Cost Interface Modification Method to Achieve High-Performance Garnet-Based Solid-State Lithium Metal Batteries. *Nano Energy.* **2022**, *91*, No. 106643.

(14) Kim, J.-S.; Yoon, G.; Kim, S.; Sugata, S.; Yashiro, N.; Suzuki, S.; Lee, M.-J.; Kim, R.; Badding, M.; Song, Z.; Chang, J. M.; Im, D. Surface Engineering of Inorganic Solid-State Electrolytes via Interlayers Strategy for Developing Long-Cycling Quasi-All-Solid-State Lithium Batteries. *Nat. Commun.* **2023**, *14*, 782.

(15) Liu, Q.; Wang, L.; He, X. Toward Practical Solid-State Polymer Lithium Batteries by in Situ Polymerization Process: A Review. *Adv. Energy Mater.* **2023**, *13*, No. 2300798.

(16) Lee, M. J.; Han, J.; Lee, K.; Lee, Y. J.; Kim, B. G.; Jung, K.-N.; Kim, B. J.; Lee, S. W. Elastomeric Electrolytes for High-Energy Solid-State Lithium Batteries. *Nature.* **2022**, *601*, 217−222.
(17) Cheng, Z.; Liu, T.; Zhao, B.; Shen, F.; Jin, H.; Han, X. Recent Advances in Organic-Inorganic Composite Solid Electrolytes for All-Solid-State Lithium Batteries. *Energy Storage Mater.* **2021**, *34*, 388−416.
(18) Zou, Z.; Li, Y.; Lu, Z.; Wang, D.; Cui, Y.; Guo, B.; Li, Y.; Liang, X.; Feng, J.; Li, H.; Nan, C.-W.; Armand, M.; Chen, L.; Xu, K.; Shi, S. Mobile Ions in Composite Solids. *Chem. Rev.* **2020**, *120*, 4169−4221.
(19) Su, Y.; Xu, F.; Zhang, X.; Qiu, Y.; Wang, H. Rational Design of High-Performance PEO/Ceramic Composite Solid Electrolytes for Lithium Metal Batteries. *Nano-Micro Lett.* **2023**, *15*, 82.
(20) Nguyen, A.-G.; Verma, R.; Song, G.-C.; Kim, J.; Park, C.-J. In Situ Polymerization on a 3D Ceramic Framework of Composite Solid Electrolytes for Room-Temperature Solid-State Batteries. *Adv. Sci.* **2023**, *10*, No. 2207744.
(21) Du, L.; Zhang, B.; Wang, X.; Dong, C.; Mai, L.; Xu, L. 3D Frameworks in Composite Polymer Electrolytes: Synthesis, Mechanisms, and Applications. *Chem. Eng. J.* **2023**, *451*, No. 138787.
(22) Wang, S.; Sun, Q.; Zhang, Q.; Li, C.; Xu, C.; Ma, Y.; Shi, X.; Zhang, H.; Song, D.; Zhang, L. Li-Ion Transfer Mechanism of Ambient-Temperature Solid Polymer Electrolyte Toward Lithium Metal Battery. *Adv. Energy Mater.* **2023**, *13*, No. 2204036.
(23) Yang, K.; Zhao, L.; An, X.; Chen, L.; Ma, J.; Mi, J.; He, Y.-B. Determining the Role of Ion Transport Throughput in Solid-State Lithium Batteries. *Angew. Chem., Int. Ed. Engl.* **2023**, *62*, No. e202302586.
(24) Reinoso, D. M.; Frechero, M. A. Strategies for Rational Design of Polymer-Based Solid Electrolytes for Advanced Lithium Energy Storage Applications. *Energy Storage Mater.* **2022**, *52*, 430−464.
(25) Xiao, P.; Yun, X.; Chen, Y.; Guo, X.; Gao, P.; Zhou, G.; Zheng, C. Insights into the Solvation Chemistry in Liquid Electrolytes for Lithium-Based Rechargeable Batteries. *Chem. Soc. Rev.* **2023**, *52*, 5255−5316.
(26) Ramos, E.; Browar, A.; Roehling, J.; Ye, J. CO_2 Laser Sintering of Garnet-Type Solid-State Electrolytes. *ACS Energy Lett.* **2022**, *7*, 3392−3400.
(27) Famprikis, T.; Canepa, P.; Dawson, J. A.; Islam, M. S.; Masquelier, C. Fundamentals of Inorganic Solid-State Electrolytes for Batteries. *Nat. Mater.* **2019**, *18*, 1278−1291.
(28) Yu, K.; Zeng, H.; Ma, J.; Jiang, Y.; Li, H.; Zhang, L.; Zhang, Q.; Shan, X.; Li, T.; Wu, X.; Xu, H.; Huang, W.; Wang, C.; Chi, S.-S.; Wang, J.; Gong, Q.; Deng, Y. High-Performance Lithium Metal Batteries Enabled by A Nano-Sized Garnet Solid-State Electrolyte Modified Separator. *Chem. Eng. J.* **2024**, *480*, No. 148038.
(29) Duan, T.; Cheng, H.; Liu, Y.; Sun, Q.; Nie, W.; Lu, X.; Dong, P.; Song, M.-K. Multifunctional Janus Layer for LLZTO/PEO Composite Electrolyte with Enhanced Interfacial Stability in Solid-State Lithium Metal Batteries. *Energy Storage Mater.* **2024**, *65*, No. 103091.
(30) Wang, R.; Yang, L.; Li, J.; Pan, S.; Zhang, F.; Zhang, H.; Zhang, S. High Rate Lithium Slurry Flow Batteries Enabled by an Ionic Exchange Nafion Composite Membrane Incorporated with LLZTO Fillers. *Nano Energy.* **2023**, *108*, No. 108174.
(31) Pan, P.; Zhang, M.; Cheng, Z.; Jiang, L.; Mao, J.; Ni, C.; Chen, Q.; Zeng, Y.; Hu, Y.; Fu, K. K. Garnet Ceramic Fabric-Reinforced Flexible Composite Solid Electrolyte Derived from Silk Template for Safe and Long-Term Stable All-Solid-State Lithium Metal Batteries. *Energy Storage Mater.* **2022**, *47*, 279−287.
(32) Ren, Z.; Li, J.; Gong, Y.; Shi, C.; Liang, J.; Li, Y.; He, C.; Zhang, Q.; Ren, X. Insight into the Integration Way of Ceramic Solid-State Electrolyte Fillers in the Composite Electrolyte for High Performance Solid-State Lithium Metal Battery. *Energy Storage Mater.* **2022**, *51*, 130−138.
(33) Guo, Y.; Pan, S.; Yi, X.; Chi, S.; Yin, X.; Geng, C.; Yin, Q.; Zhan, Q.; Zhao, Z.; Jin, F.-M.; Fang, H.; He, Y.-B.; Kang, F.; Wu, S.; Yang, Q.-H. Fluorinating All Interfaces Enables Super-Stable Solid-State Lithium Batteries by In Situ Conversion of Detrimental Surface Li_2CO_3. *Adv. Mater.* **2024**, *36*, No. 2308493.
(34) Jiao, S.; Ren, X.; Cao, R.; Engelhard, M. H.; Liu, Y.; Hu, D.; Mei, D.; Zheng, J.; Zhao, W.; Li, Q.; Liu, N.; Adams, B. D.; Ma, C.; Liu, J.; Zhang, J.-G.; Xu, W. Stable Cycling of High-Voltage Lithium Metal Batteries in Ether Electrolytes. *Nat. Energy.* **2018**, *3*, 739−746.
(35) Cai, M.; Jin, J.; Xiu, T.; Song, Z.; Badding, M. E.; Wen, Z. In-Situ Constructed Lithium-Salt Lithiophilic Layer Inducing Bi-Functional Interphase for Stable LLZO/Li Interface. *Energy Storage Mater.* **2022**, *47*, 61−69.
(36) Li, G.-X.; Jiang, H.; Kou, R.; Wang, D.; Nguyen, A.; Liao, M.; Shi, P.; Silver, A.; Wang, D. A Superior Carbonate Electrolyte for Stable Cycling Li Metal Batteries Using High Ni Cathode. *ACS Energy Lett.* **2022**, *7*, 2282−2288.
(37) Li, Y.; Qu, Q.; Lv, L.; Shao, J.; Zheng, H. A Multifunctional Additive Capable of Electrolyte Stabilization and Structure/Interphases Regulation of High-Energy Li-Ion Batteries. *Adv. Funct. Mater.* **2024**, *34*, No. 2314100.

https://doi.org/10.1021/acs.chemmater.4c02117
Chem. Mater. XXXX, XXX, XXX−XXX